Inorganic Chemistry

pubs.acs.org/IC

Article

Dissociation of Pyridinethiolate Ligands during Hydrogen Evolution Reactions of Ni-Based Catalysts: Evidence from X-ray Absorption Spectroscopy

Kathryn Ledbetter, Christopher B. Larsen, Hyeongtaek Lim, Marija R. Zoric, Sergey Koroidov, C. Das Pemmaraju, Kelly J. Gaffney, and Amy A. Cordones*

Cite This: *Inorg. Chem.* 2022, 61, 9868−9876

Read Online

ACCESS | Metrics & More | Article Recommendations | Supporting Information

ABSTRACT: The protonation of several Ni-centered pyridine-2-thiolate photocatalysts for hydrogen evolution is investigated using X-ray absorption spectroscopy (XAS). While protonation of the pyridinethiolate ligand was previously thought to result in partial dechelation from the metal at the pyridyl N site, we instead observe complete dissociation of the protonated ligand and replacement by solvent molecules. A combination of Ni K-edge and S K-edge XAS of the catalyst Ni(bpy)$(pyS)_2$ (bpy = 2,2′-bipyridine; pyS = pyridine-2-thiolate) identifies the structure of the fully protonated catalyst as a solvated $[Ni(bpy)(DMF)_4]^{2+}$ (DMF = dimethylformamide) complex and the dissociated ligands as the N-protonated 2-thiopyridone (pyS-H). This surprising result is further supported by UV−vis absorption spectroscopy and DFT calculations and is demonstrated for additional catalyst structures and solvent environments using a combination of XAS and UV−vis spectroscopy. Following protonation, electrochemical measurements indicate that the solvated Ni bipyridine complex acts as the primary electron-accepting species during photocatalysis, resulting in separate protonated ligand and reduced Ni species. The role of ligand dissociation is considered in the larger context of the hydrogen evolution reaction (HER) mechanism. As neither the pyS-H ligand nor the Ni bipyridine complex acts as an efficient HER catalyst alone, the critical role of ligand coordination is highlighted. This suggests that shifting the equilibrium toward bound species by addition of excess protonated ligand (2-thiopyridone) may improve the performance of pyridinethiolate-containing catalysts.

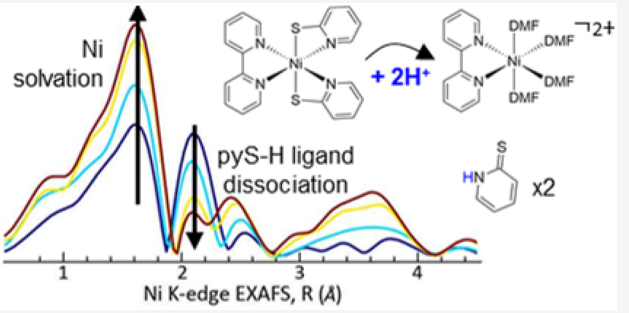

1. INTRODUCTION

Hydrogen gas, produced through the reductive side of the water-splitting reaction, is a clean fuel source and an attractive alternative to carbon-containing fuels. The energy to reduce aqueous protons to H_2 can come from electricity or light, and the efficiency of the reaction is enhanced by the use of electro- or photocatalysts.[1−5] The photocatalytic process is especially attractive as it offers a method to capture and store solar energy in the form of a clean H_2 fuel source, often by combining the catalyst with light-absorbing photosensitizers and sacrificial electron donors. While early examples of photocatalytic hydrogen evolution relied on rare and expensive noble-metal-based catalysts and photosensitizers, the development of efficient noble-metal-free catalysts is an active research field that has yielded wide-ranging molecular photocatalysts based on Ni, Co, Cu, and Fe.[4,6−10] A major challenge in this field has been to develop molecular catalysts that are robust under the light-driven reaction conditions as low turnover numbers and photodegradation of the catalyst are often observed.

A class of bioinspired pyridine-2-thiolate (pyS^-) Ni-centered complexes, including **1** and **2** (Figure 1), was found to be robust and efficient photocatalysts for H_2 evolution by Eisenberg and co-workers and is the topic of the present work.[11,12] A range of substituted $[Ni(pyS)_3]^-$ complexes (such as **2**) and heteroleptic Ni(bpy)$(pyS)_2$ complexes (where bpy = 2,2′-bipyridine, such as **1**) demonstrated large photocatalytic turnover numbers (~2000−7000 in 30 h) in combination with a fluorescein photosensitizer and triethylamine electron donor, with turnover frequencies of ~200−400 h^{-1}. It was previously demonstrated that the first step of the photocatalytic reaction mechanism is protonation, as the reduction potentials of catalysts **1** and **2** ($E_{red} \leq -1.5$ V vs SCE) preclude them from accepting electrons from the photosensitizer (fluorescein E_{red} = −1.2 V vs SCE) prior to protonation. Protonation was proposed to occur on the pyridyl N site of the pyS^- ligand

Received: January 17, 2022
Published: June 22, 2022

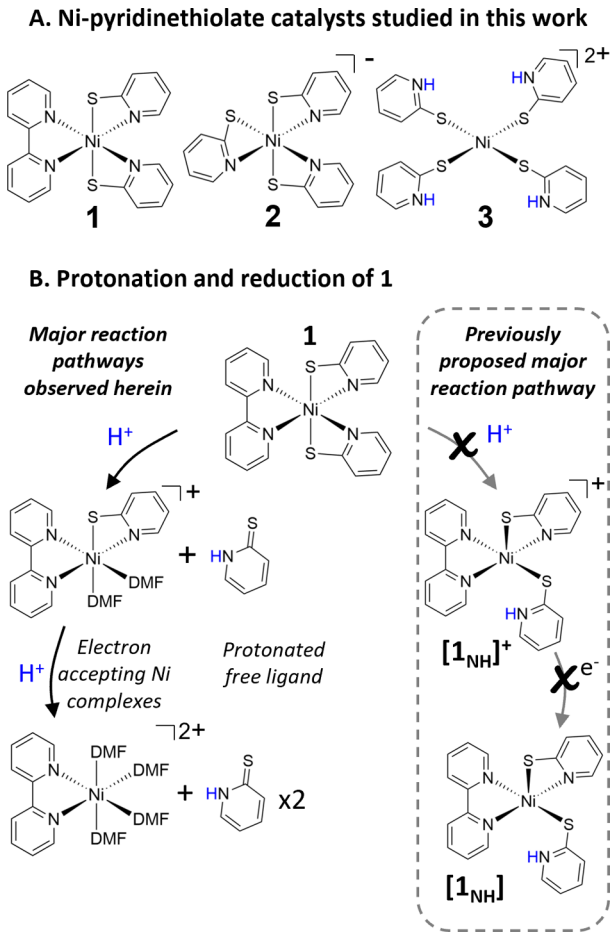

Figure 1. Photocatalysts for H_2 evolution and proton reduction scheme for $Ni(bpy)(pyS)_2$. (A) Photocatalysts **1** = $Ni(bpy)(pyS)_2$ and **2** = $[Ni(pyS)_3]^-$ and fully protonated model complex **3** = $[Ni(pyS\text{-}H)_4]^{2+}$. (B) Major reaction pathways previously proposed for protonation and reduction of **1** (right side inset), and major reaction pathways observed from this work (left side) illustrating pyS-H dissociation to form the protonated free ligand and electron-accepting solvated Ni–bipyridine species.

accompanied by partial ligand dechelation at this site, as illustrated for the previously predicted structure of the singly protonated $[\mathbf{1}_{NH}]^+$ in Figure 1B (right side). Thus, the pyS^- ligand was thought to play a critical role as a proton relay, storing protons in the vicinity of the metal center. The protonated $[\mathbf{1}_{NH}]^+$ species was proposed to then act as electron acceptor, thus completing the first proton reduction step of the hydrogen evolution reaction (HER).

While the proposed structures for the protonated catalysts were corroborated by later computational studies,[13,14] they were not isolated or characterized experimentally. The crystal structure of a related fully protonated model system $[Ni(pyS\text{-}H)_4]^{2+}$ (complex **3**, Figure 1A) provides the most compelling evidence to date for the proposed structure of $[\mathbf{1}_{NH}]^+$. Despite the lack of direct experimental evidence for the structures of the protonated (and subsequently reduced) catalyst species, the same mechanism has been invoked to describe the reactions of several more recently demonstrated Ni- and Co-centered proton and CO_2 reduction catalysts containing pyS^- or similar NS-coordinated ligands.[15−19] The mechanistic speculation for these catalysts includes pyridyl N protonation and partial dechelation at this site to form the protonated[15−17] or the reduced and protonated[15−19] catalyst species.

Protonation of the pyS^- ligand and subsequent structural changes to the catalyst are critical in understanding the catalytic mechanisms of Ni-pyS and related complexes, as these steps are thought to create an open coordination site at the metal and enable the subsequent formation of the metal–hydride or metal–carboxylate species that are important intermediates in the H_2 evolution or CO_2 reduction reactions.[11−19] Therefore, the goal of the present work is experimental characterization of the protonated form of catalyst **1**. While it is difficult to separate the mechanistic roles of the metal and ligand reaction sites using optical spectroscopy methods, element-specific core level spectroscopy is well suited to probe changes in both the electronic structure and the coordination of a specific metal or ligand atom of the catalyst upon protonation. We apply X-ray absorption spectroscopy (XAS) of the Ni and ligand S atoms to identify the structure and protonation site of the catalyst in the presence of acid and subsequently to identify further structural changes in the presence of chemical reductant. Ni K-edge XAS is sensitive to the oxidation state, coordination environment, and first coordination sphere bond lengths about the metal center.[20−23] Sulfur K-edge XAS probes the electronic structure of the pyS^- or protonated pyS-H ligands and is sensitive to the S atom protonation state and thus able to distinguish between N and S protonation[24,25] and to the metal bonding interactions of the S atom.[26−29]

On the basis of evidence from both the Ni and S XAS results, we determine that protonation of the Ni-pyS catalysts leads to complete dissociation of the protonated pyS-H ligand (dissociation of both Ni–N and Ni–S bonds) and subsequent solvation of the metal center. This result, further supported by UV–vis absorption spectroscopy and DFT calculations, prompts a reassessment of the major electron-accepting species during photocatalysis, which is identified as the solvated Ni complex. These results thus expand our understanding of the major reaction steps occurring in the protonation and reduction of Ni pyridinethiolate catalysts and are considered in the context of the HER mechanism.

2. RESULTS AND DISCUSSION

2.1. Protonation Leads to Dissociation of the pyS-H Ligand. Han et al. identified protonation as the first step of the photocatalytic hydrogen evolution mechanisms of **1** and **2**.[11,12] This was concluded on the basis of their electrochemical reduction potentials ($E_{red} \leq -1.5$ V vs SCE), which preclude electron transfer from the reduced fluorescein photosensitizer ($E_{red} = -1.2$ V vs SCE) but are thermodynamically accessible for protonated catalysts ($E_{red} \approx -1.1$ V vs SCE). We therefore set out to provide experimental evidence for the structure of the protonated catalyst **1** using a combination of UV–vis and X-ray absorption spectroscopies as described in the sections below and find that protonation of the pyS^- ligand results in its dissociation from the metal. This result is further demonstrated for catalyst **2** and for the fully protonated model complex **3** upon solvation.

2.1.1. Protonation Steps and Reversibility Determined from UV–vis Absorption Spectroscopy. To determine the number of protonation steps that **1** (containing two pyS^- ligands) undergoes, a titration was performed by adding increasing equivalents of trifluoroacetic acid (TFA) to a dimethyl sulfoxide solution of **1** (2 mM) and monitoring the

https://doi.org/10.1021/acs.inorgchem.2c00167
Inorg. Chem. 2022, 61, 9868−9876

UV−vis absorption spectrum, as shown in Figure 2. At low concentrations of TFA, one initial set of isosbestic points is observed (<0.75 equiv of TFA), while at high concentrations of TFA a second set of isosbestic points appears (>1.5 equiv of TFA). This implies the presence of three sequentially formed species with the initial isosbestic points assigned to the presence of only unprotonated and singly protonated catalyst at low TFA concentrations and the later isosbestic points assigned to the presence of only singly and doubly protonated catalyst at high TFA concentrations. We find that protonation is reversible, as the original spectrum of **1** can be recovered by the subsequent addition of excess triethylamine (Figure S1).

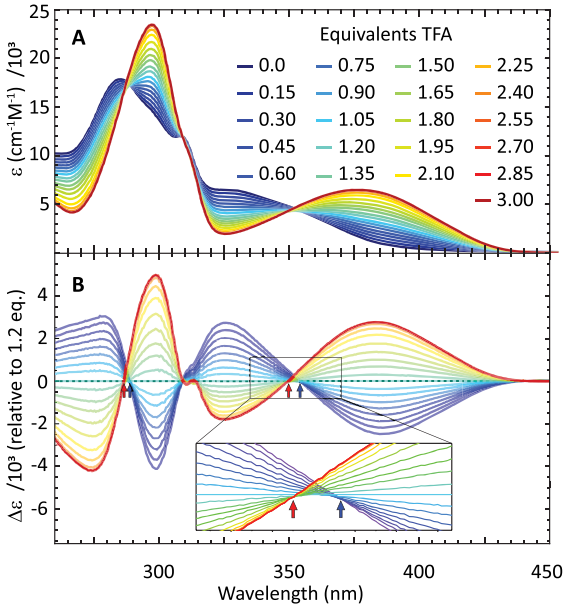

Figure 2. UV−vis absorption measured during titration of **1** with trifluoroacetic acid (TFA). (A) Spectra of **1** (2 mM in dimethyl sulfoxide) with the addition of 0−3 equiv of TFA. (B) Spectra from A after subtraction of the 1.2 equiv of TFA spectrum. Arrows mark the two sets of isosbestic points, which are also shown in greater detail in the inset.

2.1.2. Structure of the Protonated Catalyst Determined Using Ni K-Edge XAS. To identify the structural changes that accompany protonation, Ni K-edge XAS studies were performed on dimethylformamide (DMF) solutions of **1** with increasing equivalents of TFA, as shown in Figure 3. The X-ray absorption near edge structure (XANES) region (Figure 3A) exhibits a narrowing and strengthening of the strongest absorption feature and a shift of the rising edge to higher energy with added acid. Both trends have been previously associated with increasing coordination number and/or with the replacement of S-donor ligands with N- or O-donor ligands in Ni(II) complexes[23] and are thus inconsistent with the previously predicted N-protonated species $[\mathbf{1}_{NH}]^+$ (shown on the right side of Figure 1B with predicted XANES spectra shown in Figure S2).

We therefore consider the extended X-ray absorption fine structure (EXAFS) region of the spectrum, shown in Figure 3B and 3C, for a quantitative assessment of the first coordination shell bonding following protonation. Figure 3B shows the EXAFS signal as a function of wave vector (k, Å^{-1}), while Figure 3C shows the signal after Fourier transformation into R space (without phase correction). Before addition of acid, the EXAFS signal for **1** exhibits two distinct peaks in the first coordination shell, which are fit to extract the average Ni−N and Ni−S bond lengths using the ARTEMIS package,[30] as shown in Figure S3. The fit yields Ni−N bonds of the bpy and pyS ligands (4 in total) of 2.06 Å average distance and Ni−S bonds of the pyS ligands (2 in total) of 2.51 Å average distance, consistent with the values obtained from the crystal structure (2.06 and 2.53 Å, respectively).[12] The Ni−S peak decreases and the Ni−N peak increases upon addition of acid, qualitatively suggesting either the loss of S coordination or

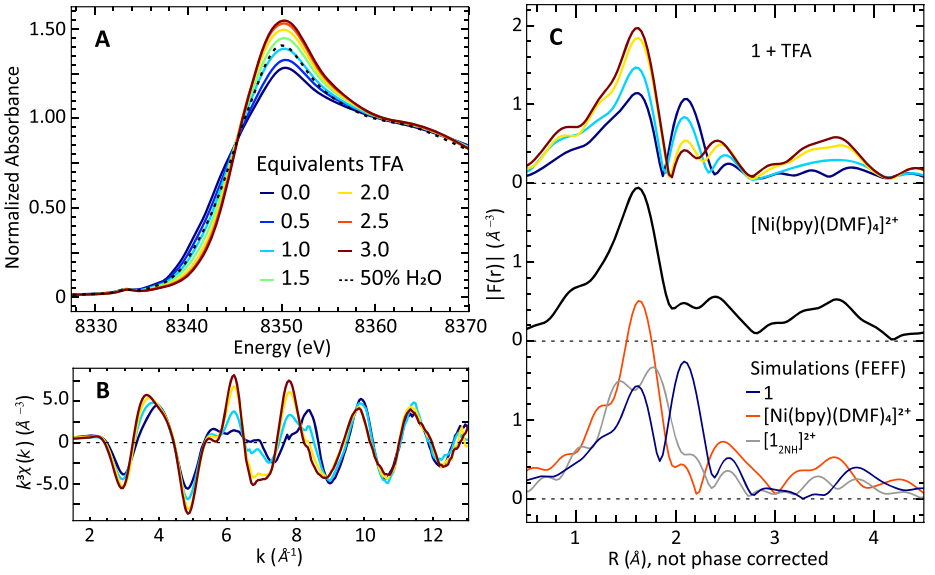

Figure 3. X-ray absorption spectroscopy of **1** with increasing equivalents of TFA. (A) Experimental Ni K-edge XANES of **1** in DMF (30 mM) with varying amounts of TFA (colored traces) and in a 1:1 DMF:H_2O mixture (black dotted trace). (B) EXAFS data for **1** in DMF with varying amounts of TFA (colored traces). (C) Fourier transform of EXAFS data shown in B and for $[Ni(bpy)(DMF)_4]^{2+}$ (black, middle trace). (Bottom traces) FEFF-simulated EXAFS for **1** (dark blue), $[Ni(bpy)(DMF)_4]^{2+}$ (red), and $[\mathbf{1}_{2NH}]^{2+}$ (gray).

https://doi.org/10.1021/acs.inorgchem.2c00167
Inorg. Chem. 2022, 61, 9868−9876

considerable contraction of the S bond (such that it overlaps with Ni−N bond distances).

To quantify the structural changes occurring upon protonation, EXAFS fits were initially attempted for the fully protonated **1** species (**1** + 3 equiv of TFA data set) using a variety of DFT-optimized starting points of **1** with two additional protons, either on pyS N or S sites, and with the pyS-H ligand remaining at least partially coordinated to Ni in all cases (Tables S11−S17). Satisfactory fits of the EXAFS data cannot be achieved using any structure where S atoms remain coordinated to or in close vicinity of the metal center. The poor fits are attributed to (1) the prediction of two first coordination sphere bonds (N and S) for all optimized structures, inconsistent with the measured EXAFS (see gray predicted EXAFS for $[\mathbf{1}_{2NH}]^{2+}$ in Figure 3C; all other optimized structures are shown in Figure S4) and (2) the measured EXAFS signal is out of phase with the expected S atom scattering signal (Figures S5 and S6). These points are discussed in detail in SI Section I. Therefore, all protonated **1** species that maintain partially coordinated pyS-H ligands can be excluded on the basis of the measured EXAFS phase and the observation of only a single first coordination sphere peak.

Given the findings above, dissociation of the pyS-H ligand is instead considered. Indeed, we find that EXAFS and XANES are both well described by a $[Ni(bpy)(DMF)_4]^{2+}$ species, implying that upon each protonation the pyS-H ligands dissociate from the metal and are replaced by two solvent molecules, as illustrated in Figure 1B (left side). There is excellent agreement between the measured EXAFS of $[Ni(bpy)(DMF)_4]^{2+}$ (Figure 3C, middle panel) and that of fully protonated **1** (i.e., **1** + 3 equiv of TFA), suggesting near unity dissociation of the protonated pyS-H ligands. In addition, excellent fits of the **1** + 3 equiv of TFA EXAFS data set in the first coordination sphere could be achieved using two Ni−N bonds (bpy ligand, 1.90 Å) and four Ni−O bonds (coordinating DMF, 2.03 Å), in agreement with the reported 2.04 Å Ni−O bonds of $[Ni(DMF)_6]^{2+}$ (Figure S7).[31] The assignment of the Ni species to $[Ni(bpy)(DMF)_4]^{2+}$ is further supported by the near-IR d−d absorption features presented below.

In addition to the experimental evidence presented above, DFT calculations also support dissociation of the pyS-H ligands, as indicated by the single-point energy calculations presented in Figure S18 and Tables S2 and S3 for optimized structures with coordinated and uncoordinated ligands. Furthermore, our findings are not unique to protonation by TFA. The XANES spectrum of **1** in a 1:1 mixture of DMF and water is shown in Figure 3A (black dashed trace). It is in excellent agreement with the spectrum of **1** + 1 equiv of TFA. Thus, a strong acid is not necessary for the pyS-H ligands to dissociate from the complex.

2.1.3. Sulfur K-Edge XAS Confirmation of pyS-H Dissociation and Protonation Site. Dissociation of the pyS-H ligands was further demonstrated using S K-edge XAS, which is sensitive to the electronic structure of the ligand S atoms, including their metal or proton bonding states.[24−29] The top panel of Figure 4 shows the measured S K-edge XANES spectra of **1** in DMF with increasing TFA (colored traces) as well as the spectrum of the free pyS-H ligand in DMF (black dashed trace). This comparison shows that the spectrum of fully protonated **1** matches that of free pyS-H ligand. Comparison with TD-DFT-simulated S K-edge spectra (bottom panel of Figure 4) further reinforces this conclusion.

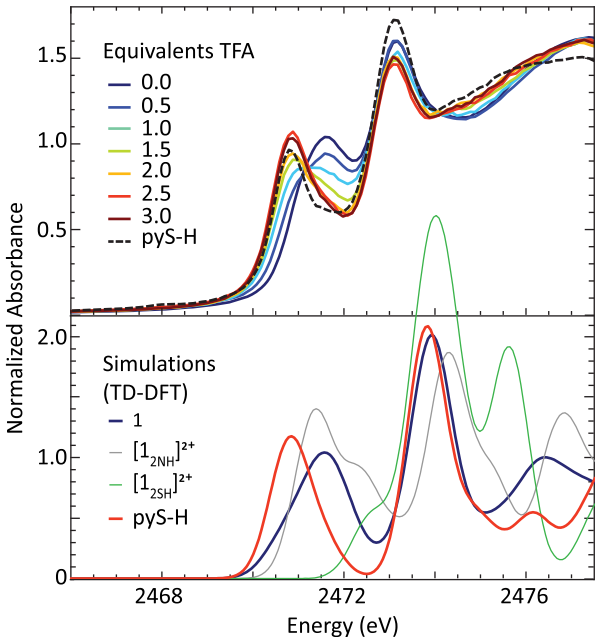

Figure 4. Sulfur K-edge XAS data (top) and TD-DFT calculations (bottom) of **1**. (Top) Spectra of **1** (30 mM DMF solutions) with varying equivalents of TFA as well as the free pySH ligand in DMF (black dashed, 40 mM). (Bottom) TD-DFT-calculated spectra of **1** (blue), $[\mathbf{1}_{2NH}]^{2+}$ (gray), $[\mathbf{1}_{2SH}]^{2+}$ (green), and pyS-H (red, N protonated).

Species maintaining Ni−S bonding, such as $[\mathbf{1}_{2NH}]^{2+}$, do not predict the observed shift in the lowest energy peak, while S-protonated species would result in the loss of this peak entirely and increased intensity in the peak at ∼2473 eV, all inconsistent with what is observed in the experiment. The presence of the lowest energy peak at ∼2471 eV indicates that the free ligand is present in the N-protonated 2-thiopyridone form, as expected in polar solvents (see Figure S8a).[24,25]

2.1.4. Spectroscopic Evidence for pyS-H Dissociation in Additional Complexes and Solvent Environments. The conclusion that protonation of the pyS^- ligand results in its dissociation from the metal is unexpected, as it has been assumed that pyS^- protonates and dechelates only at the N site with the S atoms remaining complexed to the metal. The strongest experimental evidence for the previously proposed mechanism was presented by Han et al. in the crystal structure of model complex **3**, a square planar complex with four Ni−S bonds.[12] We further investigate **3** here with additional S K-edge (Figure S8b) and Ni K-edge (Figure S9) XAS measurements. We find that both the Ni and the S XAS spectra undergo significant changes when **3** is dissolved in solution compared to when it is measured as a solid powder. When measured as a powder, the Ni K-edge EXAFS of **3** is consistent with the published crystal structure with four S bonds at 2.212 Å (Figure S10). However, upon dissolving **3** in DMF, the Ni K-edge XANES develops a more intense main absorption feature similar to that of **1** + 3 equiv of TFA, and the first-shell EXAFS peak broadens and moves to shorter bond length. We again find that the EXAFS of **3** in DMF cannot be well fit with any structure containing S atoms. Instead, it is best fit with 6 Ni−O bonds at 2.04 Å (Figure S11), in agreement with both DFT optimization (Table S22) and experimental measurement[31] of $[Ni(DMF)_6]^{2+}$. Similarly, when dissolved in solution, the S K-edge XANES spectrum of

https://doi.org/10.1021/acs.inorgchem.2c00167
Inorg. Chem. 2022, 61, 9868−9876

3 matches that of the free pyS-H ligand (Figure S8b). Thus, we conclude that although 3 has Ni−S bonds in its crystal form, its behavior in solution is similar to protonated catalyst 1: the protonated pyS-H ligands dissociate from the metal.

A thorough inspection of the UV−vis and near-IR absorption spectra of 1 and 3 further supports dissociation of the pyS-H ligand, and the spectra are used to demonstrate that this same dissociation occurs for additional solvents and catalyst 2. In the visible regime, the spectra of the fully protonated model complex 3 dissolved in DMF, ethanol, methanol, and water were all found to be equivalent to the sum of separately measured spectra of solvated Ni^{2+} and pyS-H (Figure S12), indicating that pyS-H dissociation occurs in all solvents tested.

In the near-IR regime, the d−d absorption features of 1−3 vary significantly based on the ligand environment of the metal and provide additional fingerprinting of the solvated species formed after pyS-H dissociation (Figure S13). The near-IR spectrum of the doubly protonated catalyst 1 (1+ excess TFA) in DMF matches the d−d transitions measured for $[Ni(bpy)(DMF)_4]^{2+}$ (Figure S13b). In addition, the near-IR spectra of solvated 3 and of the fully protonated catalyst 2 (2 + excess TFA) in DMF match that measured for $[Ni(DMF)_6]^{2+}$ (Figure S13a). Thus, we conclude that pyS-H ligand dissociation occurs following protonation of 2 as well.

2.2. Reduction of the Protonated Catalyst. Having established that catalyst protonation results in pyS-H ligand dissociation, a re-evaluation of the major photoinduced reduction pathway is now required. The previous work of Han et al. demonstrated that a new cathodic peak appears in the cyclic voltammograms (CVs) of 1 and 2 in the presence of a proton source at approximately −1.1 V vs SCE (approximately 0.2 V more positive than reduction of 1),[12] suggesting that the singly protonated catalyst, previously thought to be $[\mathbf{1}_{NH}]^+$, accepts electrons from the photosensitizer. Subsequent computational investigations exclusively considered species containing partially coordinated pyS-H ligands and did not investigate the potential role of ligand dissociation.[13] As we have now demonstrated that these species are not present in observable quantities following catalyst protonation, we instead consider photoreduction of the major component species existing following pyS-H dissociation.

CVs were measured for DMF solutions of catalyst 1, 1 + 10 equiv of TFA, and separate DMF solutions of the two species prevalent following protonation: $[Ni(bpy)(DMF)_4]^{2+}$ and pyS-H (Figure 5). We observe an irreversible cathodic peak at −1.93 V vs $Ag/AgNO_3$ corresponding to the first reduction of 1 and a new cathodic peak at −1.64 V vs $Ag/AgNO_3$ upon protonation of 1 with TFA, consistent with ref 12. For pyS-H, no cathodic peaks are present in the CV over the range extending to −1.8 V vs $Ag/AgNO_3$. For $[Ni(bpy)(DMF)_4]^{2+}$, an irreversible cathodic peak is observed at −1.61 V vs $Ag/AgNO_3$, consistent with the new peak observed in the CV of 1 in the presence of TFA.[12] We therefore conclude that the solvated Ni−bipyridine complex, $[Ni(bpy)(pyS)(DMF)_2]^+$ in the case of single protonation or $[Ni(bpy)(DMF)_4]^{2+}$ in the case of double protonation, is primarily reduced by the fluorescein photosensitizer.

These results indicate that the primary protonation and reduction pathways of Ni−pyS catalysts form separately protonated pyS-H free ligands and reduced solvated Ni complexes. However, upon measuring photocatalytic H_2 production, we find that neither the protonated ligand nor the solvated Ni complex acts alone as the active catalyst (see SI Section IV). Thus, the results presented here do not preclude HER mechanisms involving Ni species partially bound to pyS-H, which could exist in very small concentrations or could reform following reduction, i.e., if reduction of the Ni complex shifts the equilibrium constant for pyS-H coordination, such that recoordination of the ligand can form a $[\mathbf{1}_{NH}]$ or $[\mathbf{1}_{2NH}]^+$ species. While such a species was not isolated in this work, the S K-edge XAS spectrum was also measured for the fully protonated catalyst 1 in the presence of a chemical reductant and is consistent with a small fractional presence of a coordinated pyS-H ligand (Figure S15). Given the incomplete nature of recoordination supported by XAS, we consider the equilibrium constant of the reaction in detail in SI Section III and investigate how electrocatalytic H_2 production by $[Ni(bpy)(DMF)_4]^{2+}$ increases with added equivalents of pyS-H ligand (Figure S16).

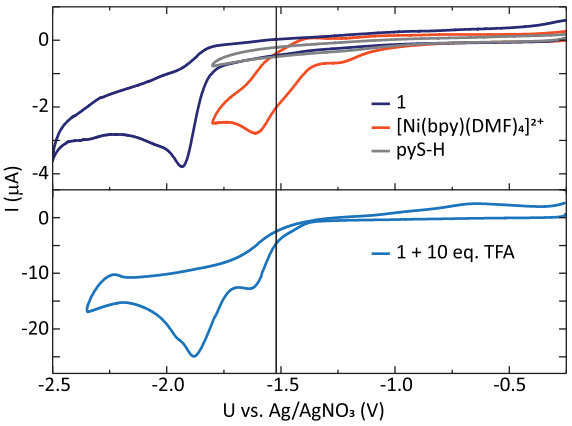

Figure 5. Cyclic voltammetry of (top) 1 (dark blue, 1 mM), $[Ni(bpy)(DMF)_4]^{2+}$ (red, 2 mM), and pyS-H ligand (gray, 2 mM), and (bottom) 1 + 10 equiv of TFA (light blue, 2 mM) measured in 0.1 M tetrabutylammonium hexafluorophosphate in DMF. Vertical line at −1.52 V vs $Ag/AgNO_3$ indicates the oxidation potential of the reduced fluorescein photosensitizer.[32]

3. CONCLUSIONS

A combination of Ni K-edge and S K-edge XAS demonstrates that protonation of the hydrogen-evolving catalyst $Ni(bpy)(pyS)_2$ results in the dissociation of the protonated pyridinethiolate ligands, leaving a solvated Ni bipyridine complex and free pyS-H ligand (in the 2-thiopyridone form). The previously predicted protonated structure $[\mathbf{1}_{NH}]^+$ with partial pyS-H ligation is not observed in measurable quantities. This surprising result of complete pyS-H dissociation is further demonstrated for additional catalyst $[Ni(pyS)_3]^-$ and structural model $[Ni(pyS\text{-}H)_4]^{2+}$ using a combination of UV−vis and X-ray absorption spectroscopies. On the basis of cyclic voltammetry we find that the solvated Ni complex is the only species present in measurable quantities that is capable of accepting electrons during photocatalysis (from reduced fluorescein dye). Thus, the first protonation and reduction of catalyst 1 primarily results in separate protonated pyS-H and reduced Ni species.

The present results demonstrate that the initial proton reduction mechanism previously proposed for Ni-pyS catalysts (Figure 1, right side) is not a major pathway. Therefore, we consider the results in the context of two different mechanistic

https://doi.org/10.1021/acs.inorgchem.2c00167
Inorg. Chem. 2022, 61, 9868−9876

scenarios for the full H_2 evolution reaction. The first possibility considered is that one of the two species present after protonation, either the solvated Ni−bipyridine complex or the free pyS-H ligand, acts as the active catalyst while the other species acts as a spectator. This is easily ruled out by the observation that catalyst **1** evolves significantly more H_2 photocatalytically than $[Ni(bpy)(DMF)_4]^{2+}$ or pyS-H alone (see SI Section IV), indicating that the HER must involve both the pyS-H ligand and the metal center.

A second scenario therefore includes an active species with partially coordinated pyS-H ligands that is critical to the HER mechanism. This can include the possibility that the originally proposed mechanism[11,12] is a minor reaction pathway, competing with the dissociation of pyS-H ligands, but is fully responsible for catalysis. Alternatively, it is possible that reduction of the solvated Ni complex changes the equilibrium constant for pyS-H coordination, forming a reduced and protonated intermediate with partially coordinated pyS-H ligands (see mechanism in Figure S14). The S K-edge XAS spectrum measured after protonation and chemical reduction is consistent with a small population of coordinated Ni-pySH species, as presented in section 2.2 above and discussed in detail in SI section III. In either case, an equilibrium between coordinated and uncoordinated pyS-H ligands is highly relevant. The implication of this equilibrium is that increasing the amount of excess pyS-H in the electro- or photocatalytic solution will enhance the rate of H_2 production by shifting the equilibrium toward bound species. This effect is explored for electrocatalysis by $[Ni(bpy)(DMF)_4]^{2+}$ in the presence of increasing amounts of pyS-H ligand in SI Section III (Figure S16). While the major pathway of pyS-H ligand dissociation has been demonstrated in the present work for complexes **1**−**3** only, the same mechanism likely plays a role for other molecular catalysts containing pyridinethiolate and related ligands, all of which propose the same mechanism of pyridyl N protonation and partial ligand dechelation.[15−19] Therefore, it is advisable to reassess the stability of those catalysts in the presence of a proton source and evaluate how ligand dissociation affects the reaction mechanism and efficiency of catalysis.

4. EXPERIMENTAL SECTION

4.1. Synthesis. Catalysts **1**, **2**, and **3** were prepared as in ref 12. The samples were characterized by UV−vis absorption and ^{1}H NMR spectroscopies, which were consistent with those previously published.[12]

$[Ni(bpy)(DMF)_4]^{2+}$ was prepared directly in DMF and used in solution.[12] A 10 mg amount bipyridine (6.4×10^{-5} mol) was dissolved in 150 μL of DMF. This was added dropwise to a stirred solution of 18.6 mg of $Ni(NO_3)_2{\cdot}6H_2O$ (6.4×10^{-5} mol) in 1 mL of DMF. The initially light green solution turned blue over 20 min of stirring.

4.2. X-ray Absorption Spectroscopy. Nickel K-edge XAS was performed at Beamlines 7-3 and 9-3 of the Stanford Synchrotron Radiation Lightsource (SSRL). Liquid samples were injected into 120 μL PEEK cells sealed with 12.7 μm Kapton tape and frozen in liquid nitrogen. During the measurement, samples were maintained at 10 K with a liquid He cryostat and positioned at 45° with respect to the incident beam. $[Ni(bpy)(DMF)_4]^{2+}$ was instead measured as a liquid at room temperature, resulting in the slight broadening observed for this EXAFS data set (Figure 3C, middle panel) compared to the others (Figure 3C, top panel). X-ray absorption spectra were collected in total fluorescence yield with a PIPS diode behind a Soller slit assembly. A Co filter (6 μm) was used to filter the elastically scattered X-rays. A Si(220) monochromator was used to scan the incident X-ray energy. Transmission through Ni foil was used as a calibration standard and was probed simultaneously with the sample by a portion of the incident beam. The peak of the first derivative of the calibration signal was set to 8333.0 eV. Each Ni K-edge XAS spectrum plotted in this work represents the average of at least two scans.

Sulfur K-edge XAS was performed at Beamline 4-3 of SSRL. Liquid samples were injected into 10 μL PEEK cells sealed with a 5 μm polypropylene film window and frozen in liquid nitrogen. During measurement, the samples were positioned at 45° from the incident beam and the temperature was kept below the freezing point of DMF (−61 °C) by a He cryostream directed at the cell from above. The cryostream also maintained a He environment between the sample and a Vortex 7-element silicon drift detector. A Si(111) monochromator was used. For calibration purposes, XAS of a sample of sodium thiosulfate powder was periodically measured, and the first peak of the absorption was set to 2472.02 eV. Each S K-edge XAS spectrum plotted in this work represents the average of at least two scans.

X-ray-induced damage was assessed from the comparison of subsequently measured spectra (measured in the same spot on the sample); if changes were observed, the X-ray flux was reduced and the spectra were remeasured in a new spot on the sample. Further evidence that X-ray radiation does not change the state of the catalyst is obtained from the discussion of the data above in (1) the consistency of metal−ligand bond lengths extracted from the EXAFS fits of **1** and **3** with their reported crystal structures and (2) the self-consistency of the XAS and UV−vis absorption spectroscopy (Figures S12 and S13) both showing pyS-H ligand dissociation upon protonation.

For both Ni and S XAS measurements, the sample concentration was 15−40 mM. Samples containing $CoCp_2^*$ were air sensitive; these samples were prepared under Ar, and the liquid cells were purged before injecting the sample and immediately freezing. The scan-to-scan variation of the normalized XAS measurement was on the order of 1% for both the Ni and S K-edge measurements shown here. However, the uncertainty of the XAS measurements is estimated at 4% based on a previous study[28] which showed that the dominant source of uncertainty in S K-edge XAS measurements of similar thiolate complexes was the choice and process of normalization and background subtraction. Here, for both Ni and S K-edge data, the background subtraction algorithm of the ATHENA package is used:[30] a linear background is fit to the pre-edge region and a quadratic function is fit to the post-edge region. Both fits are extrapolated to the tabulated absorption edge energy E_0, and the difference between the two fits at E_0 is used as the normalization constant after subtraction of the linear pre-edge background.

EXAFS fits were carried out using the ARTEMIS package.[30] Details of individual fits are given in the figures showing those fits in SI sections I and II. The k-space fit window (Hanning) was $3.0-13.x$ Å^{-1}, with x set to end the window at a node of the signal, except for solid **3**, which was 3.0−12.0 Å^{-1} due to noise at high k. Fit parameter uncertainties (as reported in Figures S3, S6, S7, and S10−11) were provided by ARTEMIS, estimated via the diagonal elements of the parameter covariance matrix of the least-squares regression, and scaled by $\sqrt{\chi^2}$ to account for the lack of a priori uncertainty estimation.[33] In addition, to evaluate the uncertainty of the reported first coordination sphere bond lengths, the standard deviation of distance fit parameters was estimated from independent fits of 6 EXAFS data sets measured for **1** in DMF: for Ni−N bonds, σ = 0.01 Å (range = 0.02 Å); for Ni−S bonds, σ = 0.01 Å (range = 0.03 Å).

4.3. XAS Modeling. Structural optimizations and S K-edge XAS simulations were carried out using the ORCA 4.1.2 package[34] with the B3P86 functional[32,35,36] (following the method of ref 13). The SMD continuum solvation model was used to model the DMF solvent.[37] For structural optimizations and single-point energy calculations, the def2-TZVP(-f) basis set[38] was used for all atoms. For the TD-DFT calculations[39,40] to simulate the S K-edge XAS, relativistic effects were included via the zero-order regular approximation (ZORA) and the ZORA-def2-TZVP basis set was used for all atoms.[41] There were

https://doi.org/10.1021/acs.inorgchem.2c00167
Inorg. Chem. 2022, 61, 9868−9876

100−200 roots calculated, and the resulting line spectra were broadened by 1.0 eV, shifted by +41.6 eV to match experiment, and scaled by a constant factor (per S atom) to match the intensity of the lowest energy absorption feature of **1**. Sample ORCA inputs are provided in SI Section VII. For each candidate structure, two spin states (singlet and triplet, or doublet and quartet, as applicable) were calculated. The lowest energy spin state was used for modeling spectra, and the results of these structural optimizations are tabulated in SI Section VI.

Modeling of the XANES region of the Ni K-edge spectra was done using the MXAN package,[42] which employs a full multiple-scattering approach and relies on the muffin-tin approximation for the shape of the potential. Although the MXAN package is capable of fitting experimental data to extract structural and nonstructural parameters, this fitting routine was not used in our calculations. Instead, the *xyz* coordinates of the molecule were provided based on the results of our DFT optimizations, and the spectrum was calculated for the fixed geometry. Nonstructural parameters were also fixed in the XANES calculations of all presented structures (muffin-tin radii overlap factor = 0.0; exchange correlation potential from the real part of the Hedin−Lunquist potential with constant energy broadening = 1.4 eV, energy-dependent broadening parameters E_S = 12 eV and A_S = 10 eV; number of scattering atoms set to the number of non-H atoms for each structure). The resulting spectra were all shifted by 8342.6 eV and scaled by a factor of 0.83 in absorbance (to best match the measured and simulated spectra of **1**).

4.4. Electrochemical Experiments. The electrochemical measurements were performed in a one-compartment cell using a Biologic SP-200 potentiostat. All cyclic voltammetry (CV) measurements were run in the standard three-electrode set up with a glassy carbon working electrode (eDAQ ET074, 0.008 cm^2 surface area), Pt wire counter electrode, and 0.1 M $Ag/AgNO_3$ nonaqueous reference electrode (MW-1085, BASi). All potentials are referenced versus this $Ag/AgNO_3$ electrode. The working electrode was polished between each CV experiment using an alumina slurry. The scan rate was 100 mV/s, and the scan direction was positive-to-negative-to-positive. Before each measurement, the electrochemical cell was purged with Ar for at least 20 min and all data was collected under inert conditions. The electrolyte was 0.1 M tetrabutylammonium hexafluorophosphate ($TBAPF_6$, recrystallized from methanol and dried in air overnight) in dry DMF, and 10 mL solutions were used for all measurements.

■ ASSOCIATED CONTENT

Supporting Information

The Supporting Information is available free of charge at https://pubs.acs.org/doi/10.1021/acs.inorgchem.2c00167.

Supporting figures and descriptions of additional UV−vis absorption spectra, XAS spectra and fits, photochemical hydrogen evolution experiments, XAS and electrochemical investigations of ligand recoordination following reduction, sample input files, and results of DFT calculations (PDF)

■ AUTHOR INFORMATION

Corresponding Author

Amy A. Cordones − *Stanford PULSE Institute, SLAC National Accelerator Laboratory, Stanford University, Menlo Park, California 94025, United States;* orcid.org/0000-0001-9897-5380; Email: acordon@slac.stanford.edu

Authors

Kathryn Ledbetter − *Stanford PULSE Institute, SLAC National Accelerator Laboratory, Stanford University, Menlo Park, California 94025, United States*

Christopher B. Larsen − *Stanford PULSE Institute, SLAC National Accelerator Laboratory, Stanford University, Menlo Park, California 94025, United States;* orcid.org/0000-0003-3006-2408

Hyeongtaek Lim − *Stanford PULSE Institute, SLAC National Accelerator Laboratory, Stanford University, Menlo Park, California 94025, United States;* orcid.org/0000-0003-3470-8296

Marija R. Zoric − *Stanford PULSE Institute, SLAC National Accelerator Laboratory, Stanford University, Menlo Park, California 94025, United States;* orcid.org/0000-0001-7296-0121

Sergey Koroidov − *Stanford PULSE Institute, SLAC National Accelerator Laboratory, Stanford University, Menlo Park, California 94025, United States*

C. Das Pemmaraju − *Theory Institute for Materials and Energy Spectroscopies, SLAC National Accelerator Laboratory, Stanford University, Menlo Park, California 94025, United States;* orcid.org/0000-0002-9016-7044

Kelly J. Gaffney − *Stanford PULSE Institute, SLAC National Accelerator Laboratory, Stanford University, Menlo Park, California 94025, United States*

Complete contact information is available at: https://pubs.acs.org/10.1021/acs.inorgchem.2c00167

Notes

The authors declare no competing financial interest.

■ ACKNOWLEDGMENTS

This work was supported by the U.S. Department of Energy, Office of Science, Basic Energy Sciences, Chemical Sciences, Geosciences, and Biosciences Division through the Early Career Research Program. K.L. was supported by a Melvin and Joan Lane Stanford Graduate Fellowship and a Stanford Physics Department fellowship. S.K. thanks The Knut and Alice Wallenberg Foundation (KAW 2014.0370) for financial support. C.D.P was supported by the U.S. Department of Energy, Office of Basic Energy Sciences, Division of Materials Sciences and Engineering, under Contract No. DE-AC02-76SF00515 through TIMES at SLAC. Use of the Stanford Synchrotron Radiation Lightsource, SLAC National Accelerator Laboratory, was supported by the U.S. Department of Energy, Office of Science, Office of Basic Energy Sciences under Contract No. DE-AC02-76SF00515. This research used resources of the National Energy Research Scientific Computing Center (NERSC), a U.S. Department of Energy Office of Science User Facility operated under Contract No. DE-AC02-05CH11231. In addition, some of the computing for this project was performed on the Sherlock cluster, and support from Stanford University and the Stanford Research Computing Center is acknowledged. The authors additionally thank Mairead Brownell and Ishaan Singh for contributing to some of the UV−vis absorption and cyclic voltammetry measurements presented in this work.

■ REFERENCES

(1) Khan, M. A.; Zhao, H.; Zou, W.; Chen, Z.; Cao, W.; Fang, J.; Xu, J.; Zhang, L.; Zhang, J. Recent Progresses in Electrocatalysts for Water Electrolysis. *Electrochemical Energy Reviews* **2018**, *1*, 483−530.

(2) Thoi, V. S.; Sun, Y.; Long, J. R.; Chang, C. J. Complexes of earth-abundant metals for catalytic electrochemical hydrogen generation under aqueous conditions. *Chem. Soc. Rev.* **2013**, *42*, 2388−2400.

(3) Pagliaro, M.; Konstandopoulos, A. G.; Ciriminna, R.; Palmisano, G. Solar hydrogen: fuel of the near future. *Energy Environ. Sci.* **2010**, *3*, 279−287.
(4) Han, Z.; Eisenberg, R. Fuel from water: The photochemical generation of hydrogen from water. *Acc. Chem. Res.* **2014**, *47*, 2537−2544.
(5) Eckenhoff, W. T.; Eisenberg, R. Molecular systems for light driven hydrogen production. *Dalton Transactions* **2012**, *41*, 13004−13021.
(6) Mazzeo, A.; Santalla, S.; Gaviglio, C.; Doctorovich, F.; Pellegrino, J. Recent progress in homogeneous light-driven hydrogen evolution using first-row transition metal catalysts. *Inorg. Chim. Acta* **2021**, *517*, 119950.
(7) Artero, V.; Chavarot-Kerlidou, M.; Fontecave, M. Splitting Water with Cobalt. *Angew. Chem., Int. Ed.* **2011**, *50*, 7238−7266.
(8) Eckenhoff, W. T. Molecular catalysts of Co, Ni, Fe, and Mo for hydrogen generation in artificial photosynthetic systems. *Coord. Chem. Rev.* **2018**, *373*, 295−316.
(9) Fukuzumi, S.; Lee, Y.-M.; Nam, W. Thermal and photocatalytic production of hydrogen with earth-abundant metal complexes. *Coord. Chem. Rev.* **2018**, *355*, 54−73.
(10) Dalle, K. E.; Warnan, J.; Leung, J. J.; Reuillard, B.; Karmel, I. S.; Reisner, E. Electro- and Solar-Driven Fuel Synthesis with First Row Transition Metal Complexes. *Chem. Rev.* **2019**, *119*, 2752−2875.
(11) Han, Z.; McNamara, W. R.; Eum, M. S.; Holland, P. L.; Eisenberg, R. A nickel thiolate catalyst for the long-lived photocatalytic production of hydrogen in a noble-metal-free system. *Angewandte Chemie - International Edition* **2012**, *51*, 1667−1670.
(12) Han, Z.; Shen, L.; Brennessel, W. W.; Holland, P. L.; Eisenberg, R. Nickel pyridinethiolate complexes as catalysts for the light-driven production of hydrogen from aqueous solutions in noble-metal-free systems. *J. Am. Chem. Soc.* **2013**, *135*, 14659−14669.
(13) Virca, C. N.; McCormick, T. M. DFT analysis into the intermediates of nickel pyridinethiolate catalysed proton reduction. *Dalton Transactions* **2015**, *44*, 14333−14340.
(14) Virca, C. N.; Lohmolder, J. R.; Tsang, J. B.; Davis, M. M.; McCormick, T. M. Effect of Ligand Modification on the Mechanism of Electrocatalytic Hydrogen Production by Ni(pyridinethiolate)3-Derivatives. *J. Phys. Chem. A* **2018**, *122*, 3057−3065.
(15) Rao, H.; Yu, W. Q.; Zheng, H. Q.; Bonin, J.; Fan, Y. T.; Hou, H. W. Highly efficient photocatalytic hydrogen evolution from nickel quinolinethiolate complexes under visible light irradiation. *J. Power Sources* **2016**, *324*, 253−260.
(16) Lee, S. E.; Nasirian, A.; Kim, Y. E.; Fard, P. T.; Kim, Y.; Jeong, B.; Kim, S.-J.; Baeg, J.-O.; Kim, J. Visible-Light Photocatalytic Conversion of Carbon Dioxide by Ni(II) Complexes with N4S2 Coordination: Highly Efficient and Selective Production of Formate. *J. Am. Chem. Soc.* **2020**, *142*, 19142−19149.
(17) Hamaguchi, T.; Kai, K.; Konishi, S.; Ando, I. Synthesis, electrochemical properties and catalytic behavior for electrochemical hydrogen production of [Ni(1,3-bis(diphenylphosphino)propane)-((2-mercaptopyridinate)-kN,S)]BF4. *Polyhedron* **2018**, *141*, 267−270.
(18) Dey, S.; Todorova, T. K.; Fontecave, M.; Mougel, V. Electroreduction of CO2 to Formate with Low Overpotential using Cobalt Pyridine Thiolate Complexes. *Angewandte Chemie - International Edition* **2020**, *59*, 15726−15733.
(19) Ahmed, M. E.; Rana, A.; Saha, R.; Dey, S.; Dey, A. Homogeneous Electrochemical Reduction of CO2 to CO by a Cobalt Pyridine Thiolate Complex. *Inorg. Chem.* **2020**, *59*, 5292−5302.
(20) de Groot, F. High-Resolution X-ray Emission and X-ray Absorption Spectroscopy. *Chem. Rev.* **2001**, *101*, 1779−1808.
(21) Yano, J.; Yachandra, V. K. X-ray absorption spectroscopy. *Photosynthesis Research* **2009**, *102*, 241.
(22) Baker, M. L.; Mara, M. W.; Yan, J. J.; Hodgson, K. O.; Hedman, B.; Solomon, E. I. K- and L-edge X-ray absorption spectroscopy (XAS) and resonant inelastic X-ray scattering (RIXS) determination of differential orbital covalency (DOC) of transition metal sites. *Coord. Chem. Rev.* **2017**, *345*, 182−208.
(23) Colpas, G. J.; Maroney, M. J.; Bagyinka, C.; Kumar, M.; Willis, W. S.; Suib, S. L.; Baidya, N.; Mascharak, P. K. X-ray Spectroscopic Studies of Nickel Complexes, with Application to the Structure of Nickel Sites in Hydrogenases. *Inorg. Chem.* **1991**, *30*, 920−928.
(24) Van Kuiken, B. E.; Ross, M. R.; Strader, M. L.; Cordones, A. A.; Cho, H.; Lee, J. H.; Schoenlein, R. W.; Khalil, M. Picosecond sulfur K-edge X-ray absorption spectroscopy with applications to excited state proton transfer. *Structural Dynamics* **2017**, *4*, 044021.
(25) Norell, J.; Eckert, S.; Van Kuiken, S.; Föhlisch, S.; Odelius, S. Ab initio simulations of complementary K-edges and solvatization effects for detection of proton transfer in aqueous 2-thiopyridone. *J. Chem. Phys.* **2019**, *151*, 114117.
(26) Glaser, T.; Hedman, B.; Hodgson, K. O.; Solomon, E. I. Ligand K-Edge X-ray Absorption Spectroscopy: A Direct Probe of Ligand-Metal Covalency. *Acc. Chem. Res.* **2000**, *33*, 859−868.
(27) Sarangi, R.; DeBeer George, S.; Rudd, D. J.; Szilagyi, R. K.; Ribas, X.; Rovira, C.; Almeida, M.; Hodgson, K. O.; Hedman, B.; Solomon, E. I. Sulfur K-Edge X-ray Absorption Spectroscopy as a Probe of Ligand-Metal Bond Covalency: Metal vs Ligand Oxidation in Copper and Nickel Dithiolene Complexes. *J. Am. Chem. Soc.* **2007**, *129*, 2316−2326.
(28) Koroidov, S.; Hong, K.; Kjaer, K. S.; Li, L.; Kunnus, K.; Reinhard, M.; Hartsock, R. W.; Amit, D.; Eisenberg, R.; Pemmaraju, C. D.; Gaffney, K. J.; Cordones, A. A. Probing the Electron Accepting Orbitals of Ni-Centered Hydrogen Evolution Catalysts with Non-innocent Ligands by Ni L-Edge and S K-Edge X-ray Absorption. *Inorg. Chem.* **2018**, *57*, 13167−13175.
(29) Cordones, A. A.; Lee, J. H.; Hong, K.; Cho, H.; Garg, K.; Boggio-Pasqua, M.; Rack, J. J.; Huse, N.; Schoenlein, R. W.; Kim, T. K. Transient metal-centered states mediate isomerization of a photochromic ruthenium-sulfoxide complex. *Nat. Commun.* **2018**, *9*, 1989.
(30) Ravel, B.; Newville, M. ATHENA, ARTEMIS, HEPHAESTUS: Data analysis for X-ray absorption spectroscopy using IFEFFIT. *Journal of Synchrotron Radiation* **2005**, *12*, 537−541.
(31) Ozutsumi, K.; Koide, M.; Suzuki, H.; Ishiguro, S. I. Solvation structure of divalent transition-metal ions in N,N-dimethylformamide and N,N-dimethylacetamide. *J. Phys. Chem.* **1993**, *97*, 500−502.
(32) Lazarides, T.; McCormick, T.; Du, P.; Luo, G.; Lindley, B.; Eisenberg, R. Making Hydrogen from Water Using a Homogeneous System Without Noble Metals. *J. Am. Chem. Soc.* **2009**, *131*, 9192−9194.
(33) Ravel, B. In *X-Ray Absorption and X-Ray Emission Spectroscopy: Theory and Applications*; van Bokhoven, J. A., Lamberti, C., Eds.; John Wiley & Sons, Ltd.: 2016; Chapter 11.
(34) Neese, F. Software update: the ORCA program system, version 4.0. *Wiley Interdiscip. Rev.: Comput. Mol. Sci.* **2018**, *8*, e1327.
(35) Miehlich, B.; Savin, A.; Stoll, H.; Preuss, H. Results obtained with the correlation energy density functionals of becke and Lee, Yang and Parr. *Chem. Phys. Lett.* **1989**, *157*, 200−206.
(36) Perdew, J. P. Density-functional approximation for the correlation energy of the inhomogeneous electron gas. *Phys. Rev. B* **1986**, *33*, 8822−8824.
(37) Marenich, A. V.; Cramer, C. J.; Truhlar, D. G. Universal Solvation Model Based on Solute Electron Density and on a Continuum Model of the Solvent Defined by the Bulk Dielectric Constant and Atomic Surface Tensions. *J. Phys. Chem. B* **2009**, *113*, 6378−6396.
(38) Weigend, F.; Ahlrichs, R. Balanced basis sets of split valence, triple zeta valence and quadruple zeta valence quality for H to Rn: Design and assessment of accuracy. *Phys. Chem. Chem. Phys.* **2005**, *7*, 3297−3305.
(39) Jamorski, C.; Casida, M. E.; Salahub, D. R. Dynamic polarizabilities and excitation spectra from a molecular implementation of time-dependent density-functional response theory: N2 as a case study. *J. Chem. Phys.* **1996**, *104*, 5134−5147.

https://doi.org/10.1021/acs.inorgchem.2c00167
Inorg. Chem. 2022, 61, 9868−9876

(40) Hirata, S.; Head-Gordon, M. Time-dependent density functional theory within the Tamm-Dancoff approximation. *Chem. Phys. Lett.* **1999**, *314*, 291−299.
(41) van Lenthe, E.; Snijders, J. G.; Baerends, E. J. The zero-order regular approximation for relativistic effects: The effect of spin-orbit coupling in closed shell molecules. *J. Chem. Phys.* **1996**, *105*, 6505−6516.
(42) Benfatto, M.; Della Longa, S.; Natoli, C. R. The MXAN procedure: A new method for analysing the XANES spectra of metalloproteins to obtain structural quantitative information. *J. Synchrotron Radiat.* **2003**, *10*, 51−57.

https://doi.org/10.1021/acs.inorgchem.2c00167
Inorg. Chem. 2022, 61, 9868−9876